Improved Scheme for Estimating the Embedded Gate Resistance to Reproduce SiC MOSFET Circuit Performance

Shogo Ogawa, Taketoshi Tanaka, and Ken Nakahara, *Senior Member, IEEE*

***Abstract*—The intrinsic gate resistance (R_{g_in}), which is a novel resistance factor embedded in transistors, was determined for silicon carbide (SiC) metal–oxide–semiconductor field-effect transistors (MOSFETs). The study demonstrated that R_{g_in} is overestimated in the conventional measurement scheme due to the contact resistance R_{sp} between p-type SiC and the source electrode. Here, 6.7 mΩ·cm^2 was measured for R_{sp} using the transfer length method (TLM), and R_{g_in} = 9 Ω was the revised value, unlike the conventional value of 25 Ω. This improved R_{g_in} provides better-simulated switching waveforms in a double-pulse test (DPT) with a SiC MOSFET; however, the method requires detailed knowledge of the target device. Accordingly, we developed another measurement scheme without such prerequisites. In this scheme, three types of impedance (Z) were measured: Z between the drain (D) and source terminal (S), and two Z_s between the gate and S, with DS left open and short. From these results, R_{g_in} was determined to be 8.8 Ω with other device parasitic parameters simultaneously.**

***Index Terms*—Contact resistance, internal gate resistance, metal–oxide–semiconductor field-effect transistor (MOSFET), silicon carbide (SiC).**

I. Introduction

SILICON carbide (SiC) metal–oxide–semiconductor field-effect transistors (MOSFETs) are the most promising for next-generation power devices because of their excellent characteristics, including high breakdown voltage tolerance and high-speed switching [1], [2]. High-speed switching operations cause low power loss in switching power supplies; however, they simultaneously deteriorate the electromagnetic compatibility (EMC) of the supplies [3]. Accordingly, a reliable method for optimizing the switching processes of the transistors used in power applications is required.

The gate resistance (R_g) is a circuit element that is useful for adjusting transistor switching processes. R_g comprises R_{g_ext} and R_{g_in}, which are the resistance elements existing outside the transistor and an intrinsic resistance factor embedded in a transistor chip, respectively. Power application engineers cannot adapt R_{g_in}; thus, device manufacturers should be responsible for providing an appropriate R_{g_in}.

Manuscript received 10 April 2023; revised 7 June 2023 and 12 July 2023; accepted 15 July 2023. Date of publication 1 August 2023; date of current version 23 August 2023. The review of this article was arranged by Editor S. N. E. Madathil. *(Corresponding author: Shogo Ogawa.)*

The authors are with the Research and Development Center, ROHM Company Ltd., Kyoto 615-8585, Japan (e-mail: shogo.ogawa@mnf.rohm.co.jp).

Color versions of one or more figures in this article are available at https://doi.org/10.1109/TED.2023.3297567.

Digital Object Identifier 10.1109/TED.2023.3297567

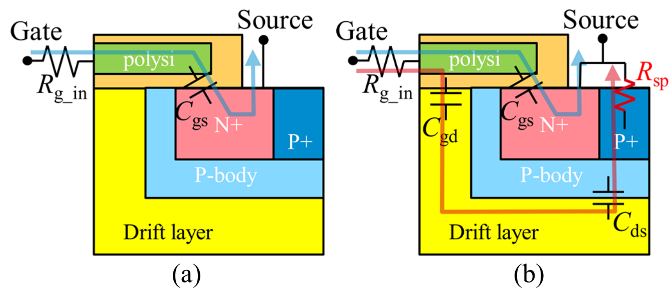

Fig. 1. Unit-cell structure around the source contact of a SiC MOSFET. Current flows that should be considered for the measurement of R_{g_in} are also provided in (a) conventional case and (b) case of nonnegligible R_{sp}.

R_{g_in} is frequently provided on the device datasheet as the real part of the impedance, measured at 1 MHz between the gate (G) and source terminals (S), with an open drain terminal (D). The real part is calculated under the assumption that the input capacitances of the transistor and R_{g_in} are serially connected [4]. This method is widely applied to SiC and Si MOSFETs [5], [6], [7].

However, R_{g_in} of SiC MOSFETs reportedly differs from R_{g_cir}, which denotes R_{g_in} expected from the switching behavior of a transistor [8]. Fig. 1(a) shows the standard unit structure of a SiC MOSFET and the current flow path conventionally assumed in R_{g_in} measurements [4], [5]. R_{g_in} coincides with R_{g_cir} if the path is valid. However, this is not the case for SiC MOSFETs because the contact resistance R_{sp} between p-SiC and the source contact is not negligible.

According to [9] and [10], R_{sp} in SiC MOSFETs is approximately 4.0 × 10^{-3} Ω·cm^{-2}, and this value is larger by more than two orders of magnitude than the value of 1.0 × 10^{-5} Ω·cm^{-2} for Si MOSFETs [11]. Thus, the current path, denoted by the red line in Fig. 1(b), competes impedance-wise with the conventional path. This indicates that the conventional methodology of measuring R_{g_in} must be rebuilt.

In this article, the estimation of R_{sp} using the transfer length method (TLM) is described in Section II. The measurement results for R_{sp} are validated from multiple perspectives in Section III. In Section IV, the subtraction of R_{sp} from R_{g_cir} is

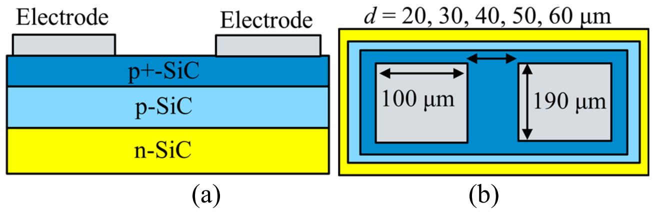

Fig. 2. (a) Cross-sectional view and (b) plane view of the TLM device for measuring R_{sp} and R_{sh}.

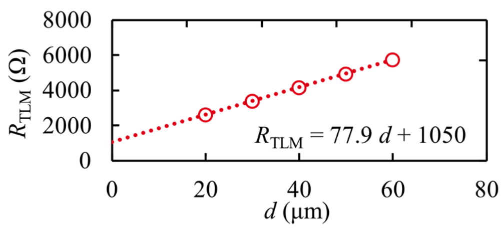

Fig. 3. R_{TLM}–d characteristics of the TLM device.

demonstrated. Circuit simulations using this newly determined R_{g_in} reproduced the measured switching behaviors better than those using the conventional R_{g_in} on device datasheets. Section V presents a revised measurement method to determine R_{g_in} based on the impedance characteristics. Section VI concludes this article.

II. Measurement of R_{SP}

R_{sh}, i.e., the sheet resistance of a p-type SiC, and R_{sp} were experimentally estimated. Fig. 2(a) and (b) shows the TLM patterns in the cross- and plane-sectional views, respectively [12]. These TLM structures were fabricated on an n-type 4H-SiC epitaxial layer implanted with aluminum ions (Al^+) and a distance between the metal pads, d, ranging from 20 to 60 μm in 10-μm steps. The acceptor ion densities of the p-SiC and p+-SiC regions were approximately 2×10^{16} and 5×10^{19} cm^{-3}, respectively. The TLM sample adopted for this measurement was manufactured for process-control monitoring of the product wafer of SiC MOSFETs (SCT2450KE, ROHM Company Ltd.).

Fig. 3 shows the measured R_{TLM}, i.e., the resistance between the pads, as a function of d. The slope of the observed linear correlation represents R_{sh}, and R_{sp} corresponds to the vertical intercept of the graph. The estimated R_{sh} and R_{sp} were 1.48×10^4 Ω/sq. and 6.7 mΩ·cm^2, respectively.

Fig. 4(a) shows the TLM pattern to introduce R_{sh} and R_{sp} modeled in a TCAD simulation (Sentaurus Device, Synopsys Inc.), where we applied the incomplete ionization model for the implanted Al^+ [13] with an activation energy ($\Delta E_{A,0}$) of 0.38 eV [14]. R_{sp} was considered to have a fixed resistance of 6.7 mΩ·cm^2. Fig. 4(b) shows the current–voltage (I–V) characteristics of the TLM samples and their simulated counterparts. The simulation setup conditions reproduced R_{sh} and R_{sp}. Accordingly, we used these setups in subsequent TCAD simulations.

III. Validation of the Experimental R_{SP}

The magnitude of R_{sp} crucially influences R_{g_in} estimation; thus, we examined its consistency using other methods. One of these was the drain current as a function of the drain voltage characteristics in the third quadrant, (I_r–V_r), and the alternating

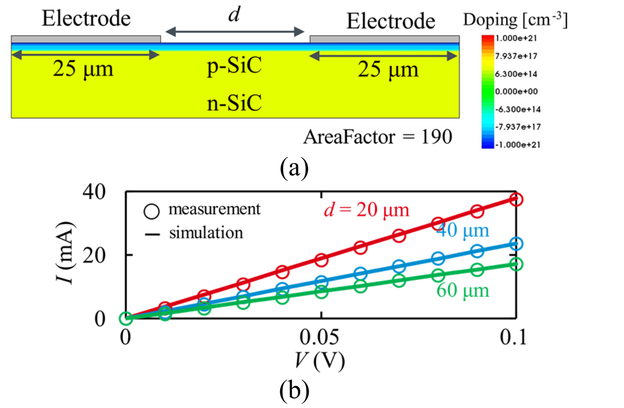

Fig. 4. (a) TCAD-modeled TLM pattern for simulating R_{sh} and R_{sp}. (b) I–V characteristics of the TLM device. The open circles and solid lines denote the experimental and simulated results, respectively.

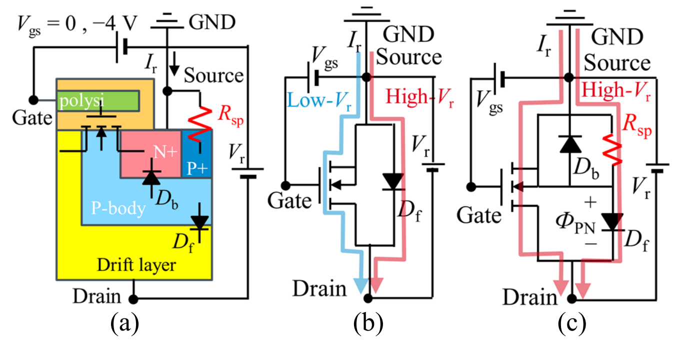

Fig. 5. (a) Wiring setup for I_r–V_r measurements and simulations. The change in current flow depending on V_f for (b) negligible R_{sp} and (c) nonnegligible R_{sp}.

current (ac) characteristics between D and S. The TCAD model of the SiC MOSFET was the same as that reported previously [15].

Fig. 5(a) shows the wiring setup for I_r–V_r measurements; the circuit elements embedded in the SiC MOSFET are defined therein. Fig. 5(b) and (c) shows the equivalent circuits with and without R_{sp}, respectively. According to [9], I_r depends on V_{gs} because of the current contribution of the MOS to I_r if R_{sp} is nonnegligible, as shown in Fig. 5(b) and (c). This trend depends on whether R_{sp} can be ignored at high-V_r values when V_r is larger than the built-in potential (Φ_{p-n}) of the p-n junction between the drift layer and the p-body. A low V_r means V_r below Φ_{p-n}. According to [16], Φ_{p-n} is 2.7 V.

Fig. 6(a) and (b) shows the measured (open circles) and simulated (solid lines) I_r–V_r characteristics under $V_{gs} = 0$ V (in red) and -4 V (in blue). The simulation results for $R_{sp} = 0$ and 6.7 mΩ·cm^2 are shown in Fig. 6(a) and (b), respectively. $R_{sp} = 0$ Ω·cm^2 failed to reproduce the measured results, as shown in Fig. 6(a). In stark contrast, $R_{sp} = 6.7$ mΩ·cm^2 accurately reflected the measurement results. This result was evidence that $R_{sp} = 6.7$ mΩ·cm^2 is valid for SiC MOSFETs.

Furthermore, Z_{DS}, i.e., the impedance between D and S, was analyzed. Fig. 7(a) shows the wiring setup for this, and the related circuitry elements embedded in the SiC MOSFET are also defined therein. Fig. 7(b) and (c) shows the equivalent circuits with and without R_{sp}, respectively. As shown in Fig. 7(b), the ac signal flowed independently of the V_{ac} frequency (f_{ac}) without R_{sp} because C_{ds} always provides the lowest impedance path. However, in the presence of R_{sp}, the

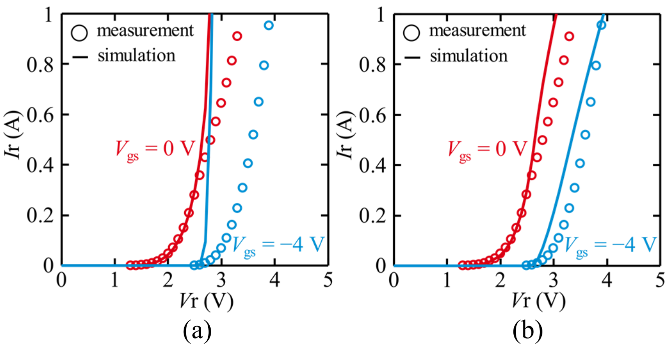

Fig. 6. (a) I_r–V_r characteristics with R_{sp} = 0 Ω·cm^2 and (b) R_{sp} = 6.7 Ω·cm^2. Open circles and solid lines denote the measurement and simulation results, respectively. Red and blue show the results with V_{gs} = 0 V and V_{gs} = −4 V being applied, respectively.

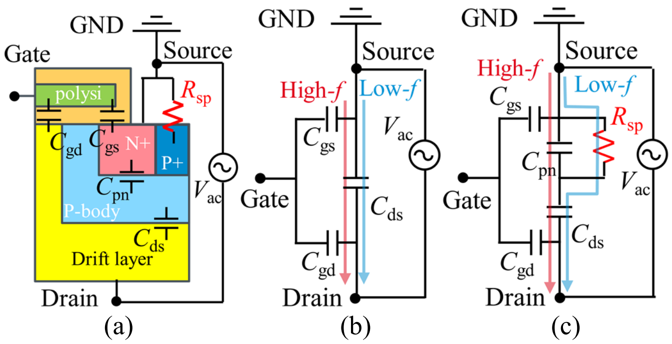

Fig. 7. (a) Wiring setup to obtain Z_{DS}–f_{ac} correlations. The change in current flow, depending on f_{ac}, for (b) negligible R_{sp} and (c) nonnegligible R_{sp}.

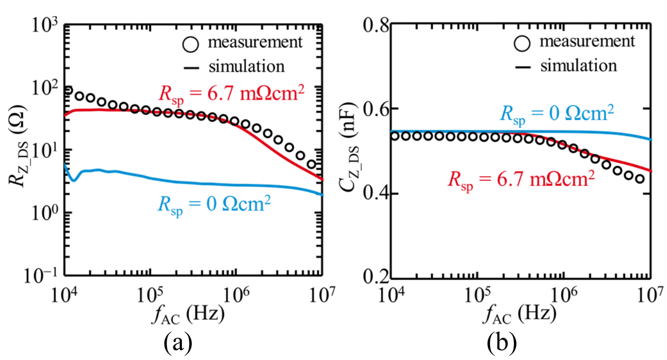

Fig. 8. (a) R_{Z_DS} and (b) C_{Z_DS} functions of f_{ac}. Open circles and solid lines represent the measured and simulated results, respectively. Red and blue indicate the results for no R_{sp} and R_{sp} = 6.7 mΩ·cm^2, respectively.

signal path varied with f_{ac} [Fig. 7(c)] because a higher f_{ac} increases the impedance of R_{sp} and lowers that of C_{pn}. Thus, the Z_{DS}–f_{ac} correlation depends on the magnitude of R_{sp}, implying that this correlation can be used to estimate R_{sp}.

Fig. 8(a) and (b) shows the measured (open circles) and simulated (solid lines) results for $R_{Z\_DS} = \mathrm{Re}(Z_{DS})$ and $C_{Z\_DS} = |\{\mathrm{Im}(Z_{DS} 2\pi f_{ac})\}^{-1}|$ as a function of f_{ac}. The simulations were performed for R_{sp} = 0 and 6.7 mΩ·cm^2. From Fig. 7(a) and (b), both of the simulated R_{Z_DS} and C_{Z_DS} for R_{sp} = 6.7 mΩ·cm^2 reproduced the measured counterparts over $f_{ac} = 10^4$–10^7 Hz, whereas those for R_{sp} = 0 Ω·cm^2 did not. In addition, the simulated R_{Z_DS} and C_{Z_DS} for R_{sp} = 6.7 mΩ·cm^2 successfully followed the downward trend experimentally observed at $f_{ac} \geq 10^6$ Hz. This decrease reflected the change in the signal path, as shown in Fig. 7(c).

The results in this section support the validity of R_{sp} = 6.7 mΩ·cm^2; therefore, this R_{sp} value was used in the simulation described in the following section.

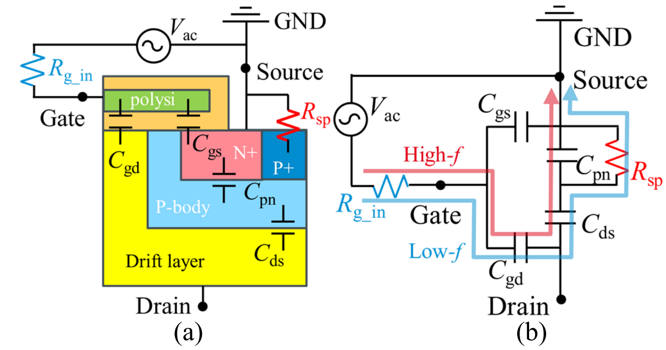

Fig. 9. (a) Wiring setup for obtaining Z_{GS}–f_{ac} curves. (b) Equivalent circuit showing the change in current flow depending on f_{ac}.

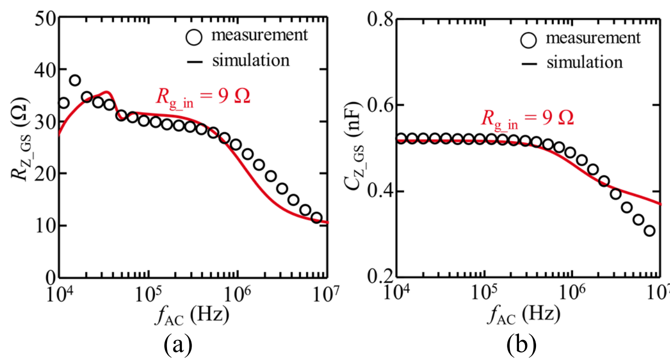

Fig. 10. AC characteristics between GS terminals. Circles and lines denote the measurement and simulation results of (a) R_{Z_GS} and (b) C_{Z_GS}.

IV. R_{G_in} Extraction and Its Effects

Fig. 9(a) shows the wiring setup for measuring and simulating the impedance between G and S (Z_{GS}). The circuitry elements embedded in the SiC MOSFET are also defined therein. Fig. 9(b) shows the equivalent circuit. As shown in Fig. 9(b), R_{g_in} always lay along the current path and consequently functioned as a constant element in Z_{GS}. Accordingly, R_{g_in} could be determined as a fitting parameter for Z_{GS}–f_{ac} characteristics.

Fig. 10(a) and (b) shows the simulation (red solid lines) and measurement (open circles) results for $R_{Z\_GS} = \mathrm{Re}(Z_{GS})$ and $C_{Z\_GS} = |\{\mathrm{Im}(Z_{GS} \cdot 2\pi f_{ac})\}^{-1}|$ as a function of f_{ac}, including the effects of R_{sp} = 6.7 mΩ·cm^2. R_{g_in} = 9 Ω provided the best fitting result, whereas R_{g_in} on the datasheet of SCT2450KE was 25 Ω.

The switching behavior of the transistors is important; hence, R_{g_in} was verified using the extent to which it reproduces the switching behavior of the SiC MOSFET. Fig. 11 shows a schematic of the double-pulse test (DPT), where the device model of a SiC MOSFET and the circuit components were the same as those previously reported [17]. This device model reproduced the I_d–V_d and C–V_d characteristics of the SiC MOSFET adopted in the DPT, as shown in Fig. 12(a) and (b), where I_d and V_d denote the drain current

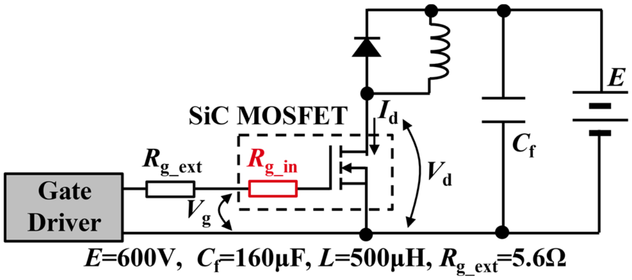

Fig. 11. Schematic of DPT. The circuit constants are given at the bottom of the diagram. R_{g_ext} denotes a resistor mounted in this DPT circuit.

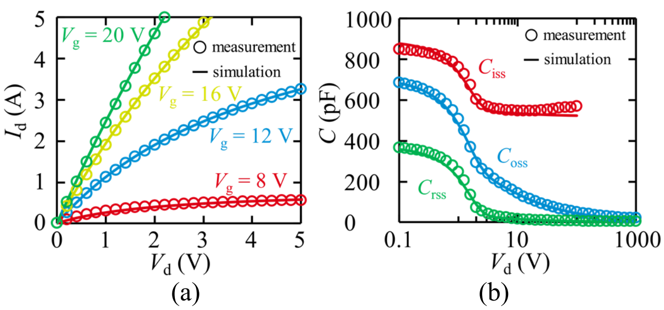

Fig. 12. (a) I_d–V_d and (b) C–V_d characteristics. Open circles and solid lines denote the measurement and simulated characteristics.

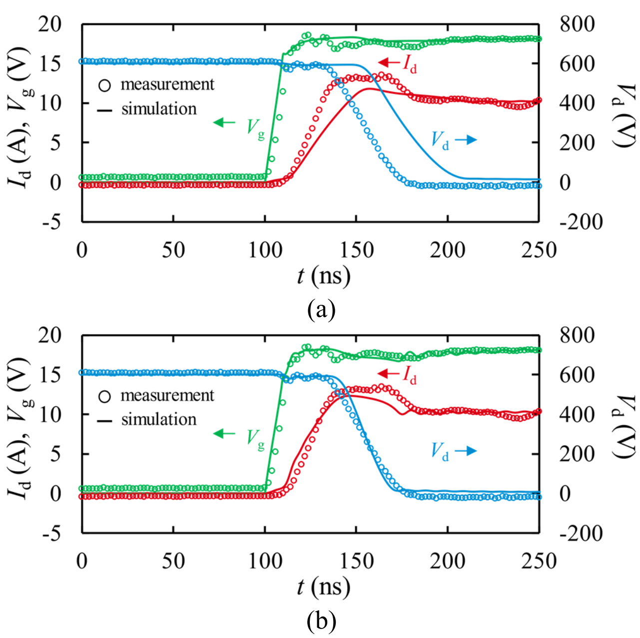

Fig. 13. Turn-on switching waveforms. Open circles and solid lines denote the experimental and simulated results, respectively, for (a) R_{g_in} = 25 Ω and (b) R_{g_in} = 9 Ω.

and voltage, respectively. C denotes the input (C_{iss}), output (C_{oss}), and feedback capacitances (C_{rss}) of the device. These characteristics confirm the validity of the circuit simulations.

The measured turn-on waveforms are superimposed on the simulated counterparts in Fig. 13(a) and (b) for R_{g_in} = 25 Ω and R_{g_in} = 9 Ω, respectively. The quantitative index of the extent to which the simulated results agreed with their experimental counterparts was the relative root-mean-square (rRMS) error, as defined in [18].

Fig. 14(a) and (b) shows the measured and simulated turn-on waveforms, respectively. Regarding R_{g_in} = 25 Ω, the simulated V_d and I_d altered with a lag behind the observed values. In stark contrast, R_{g_in} = 9 Ω provided better-quality

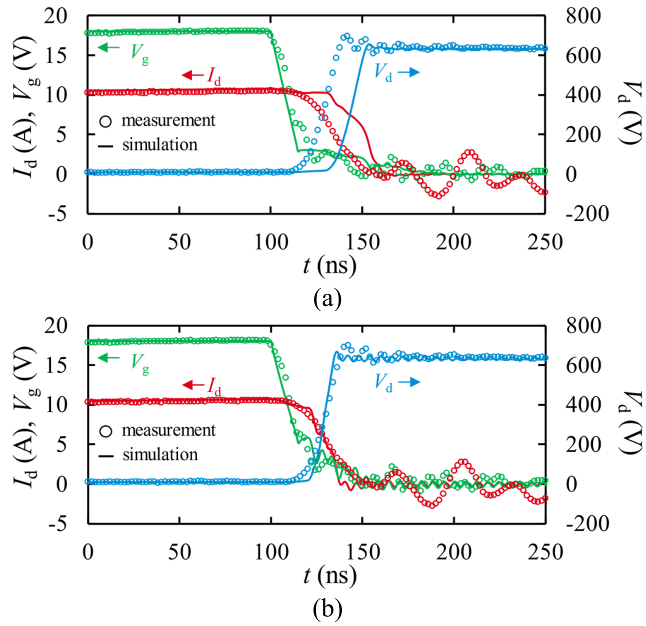

Fig. 14. Turn-off switching waveforms. Open circles and solid lines denote the experimental and simulated results for (a) R_{g_in} = 25 Ω and (b) R_{g_in} = 9 Ω, respectively.

TABLE I
RELATIVE RMS ERROR AT TURN-ON AND TURN-OFF

	Turn-on (%)		Turn-off (%)	
R_{g_in}	25 Ω	9 Ω	25 Ω	9 Ω
V_g	8.7	7.0	23.8	17.1
V_d	45.2	7.9	54.2	9.6
I_d	18.8	11.4	41.3	14.3

simulation results. This result was also the same for the turn-off behavior, as shown in Fig. 14(c) and (d). Table I lists the rRMS errors of V_g (gate-to-source voltage), V_d, and I_d for the turn-on and turn-off waveforms. R_{g_in} = 9 Ω provided a better rRMS than R_{g_in} = 25 Ω. These results prove that the newly determined R_{g_in} method better reflects R_{g_cir}, implying that application engineers should use the proposed value.

V. R_{G_in} DETERMINATION METHOD USING ONLY CIRCUITOUS MEASUREMENTS

The aforementioned method for estimating R_{g_in} requires that the structure of the target device is known; however, less prior knowledge is more useful. Therefore, we propose a measurement scheme to determine R_{g_in} using only circuitous measurements.

Fig. 15(a) shows all the decomposed circuitry elements embedded in the unit structure of the SiC MOSFET. In addition, the symbols for the elements are defined. Fig. 15(b) shows the equivalent circuit. There are ten parameters in total; however, R_{epi} is more negligible than the other resistance factors because of its typical value of 1 mΩ·cm^2 [11]. In addition, from R_{sh}, the resistance of the p-body region is also negligible because it is comparable to R_{epi}. Thus, there are nine unknown parameters. C_{gd}, C_{ds}, and C_{gs} are obtained from $C - V_d$ measurements. C_{gs} is equal to $C_{gsn} + \{(C_{gsp})^{-1} + (C_{gsd})^{-1}\}^{-1}$, and when two of C_{gsp}, C_{gsn}, and C_{gsd} are known, the remaining one can be determined. R_{ch} should be included because the magnitude of R_{ch} is approximately 10^7 Ω [10]. This value is not negligible compared to the

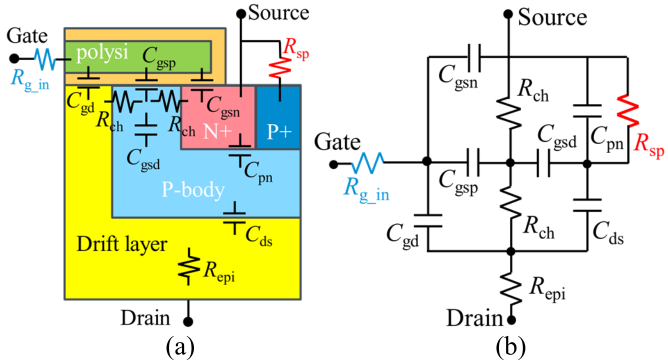

Fig. 15. (a) Unit structure of a SiC MOSFET and all embedded decomposed circuitry elements and (b) its equivalent circuit.

TABLE II
DEFINITION OF SYMBOLS IN (1)–(3)

Symbol	Corresponding physical quantity (j: imaginary unit, ω:$2\pi f_{AC}$)
D_a	$(j\omega C_{gd})^{-1}$
D_b	$(j\omega C_{gsp})^{-1}$
D_c	$(j\omega C_{gsn})^{-1}$
D_d	R_{ch}
D_e	$(j\omega C_{gsd})^{-1}$
D_f	$(j\omega C_{ds})^{-1}$
D_g	$(R_{sp}{}^{-1} + j\omega C_{pn})^{-1}$
Y_{klm}	$D_k D_l (D_k + D_l + D_m)^{-1}$
$Y(X,Y,Z)$	$XY(X+Y+Z)^{-1}$

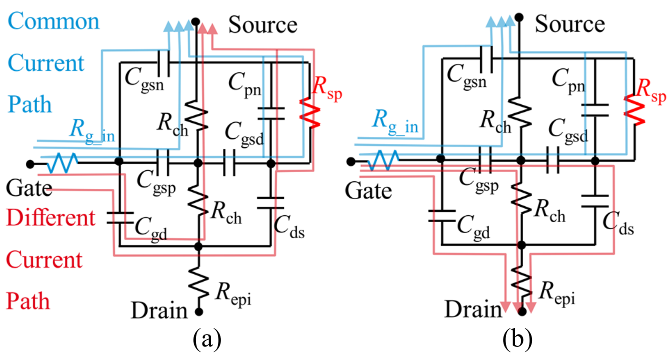

Fig. 16. Current paths for measuring (a) Z_{GSO} and (b) Z_{GSS}.

impedances of other components. Consequently, the number of unknown parameters is reduced to six: R_{g_in}, R_{sp}, R_{ch}, and C_{pn}, and two from C_{gsp}, C_{gsn}, and C_{gsd}. This implies that six mutually independent equations are required to determine these six parameters.

We adopt Z_{DS} and Z_{GS} to establish these six equations. Z_{ds} is measured using the configuration shown in Fig. 7(a), i.e., the impedance between D and S with open G. Two types of Z_{GS} are measured: open DS (Z_{GSO}) and short DS (Z_{GSS}). The ac signal flows for measuring Z_{GSO} and Z_{GSS} are shown in Fig. 16(a) and (b), respectively. The blue lines indicate the signal paths shared by Z_{GSO} and Z_{GSS}, and the red lines indicate the paths that are dependent on whether DS is open or short. This signal path difference leads to clear impedance differences between Z_{DS}, Z_{GSO}, and Z_{GSS}, thereby creating six equations to determine the aforementioned unknown parameters. Z_{DS}, Z_{GSO}, and Z_{GSS} can be expressed

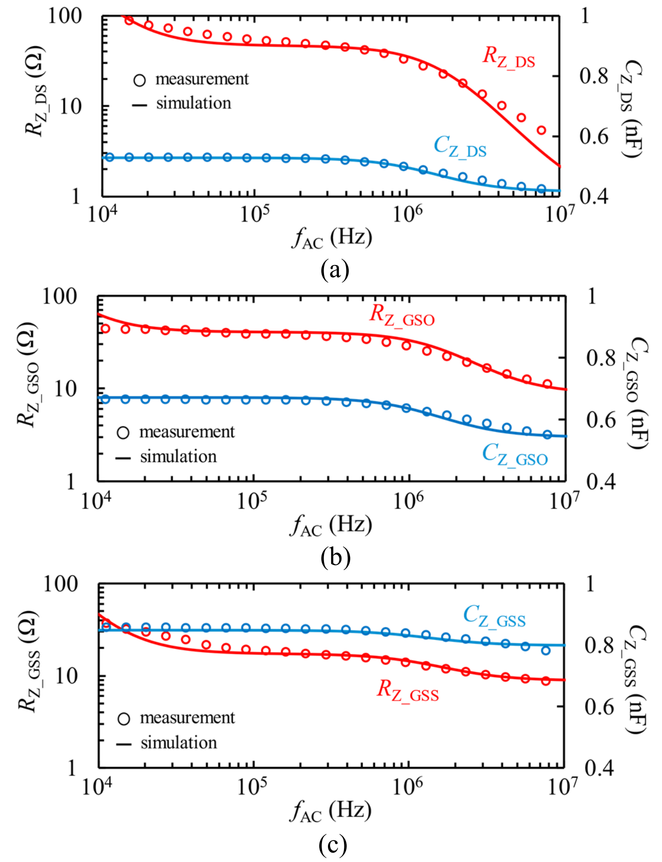

Fig. 17. (a) Z_{DS}, (b) Z_{GSO}, and (c) Z_{GSS} as functions of f_{ac}. The open circles and solid lines denote the measured and fit results, respectively.

TABLE III
FIT PARAMETERS

Symbol	Fitted results
C_{gd}	0.34 nF
C_{gsp}	0.63 nF
C_{gsd}	0.62 nF
C_{gsn}	0.20 nF
R_{ch}	6.11×10^6 Ω
C_{ds}	0.32 nF
C_{pn}	1.28 nF
R_{sp}	63.2 Ω
R_{g_in}	8.8 Ω
E_r	0.20

by (1)–(3), as shown at the top of the next page. The symbols used are listed in Table II. The real and imaginary parts of (1)–(3) provide six equations. Therefore, the unknown parameters can be uniquely determined by minimizing the rms error E_r as given by the following equation:

$$E_r = \sqrt{\sum_{i,x}\left\{\left(\log\frac{R_{Z\_x\_c,i}}{R_{Z\_x\_m,i}}\right)^2 + \left(C_{Z\_x\_c,i} - C_{Z\_x\_m,i}\right)^2\right\}} \quad (4)$$

where i, x, c, and m denote the data point; DS, GSO, or GSS; calculated; and measured, respectively.

Fig. 17(a)–(c) shows the measured Z_{DS}, Z_{GSO}, and Z_{GSS} values of SCT2450KE, respectively. In addition, these figures show the curves determined to minimize E_r for (1)–(3). Table III presents the parameters determined using E_r and the value of E_r. R_{g_in} is 8.8 Ω and very close to 9 Ω. This

$$Z_{\mathrm{DS}} = Y\left(Y_{\mathrm{dab}}, D_{\mathrm{f}} + Y_{\mathrm{egd}}, Y_{\mathrm{bda}} + Y_{\mathrm{deg}}\right) + \left\{\frac{1}{D_{\mathrm{c}} + Y_{\mathrm{abd}} + Y\left(Y_{\mathrm{bda}} + Y_{\mathrm{deg}}, Y_{\mathrm{dab}}, D_{\mathrm{f}} + Y_{\mathrm{egd}}\right)} + \frac{1}{Y_{\mathrm{gde}} + Y\left(D_{\mathrm{f}} + Y_{\mathrm{egd}}, Y_{\mathrm{bda}} + Y_{\mathrm{deg}}, Y_{\mathrm{dab}}\right)}\right\}^{-1} \quad (1)$$

$$Z_{\mathrm{GSO}} = \left[\frac{1}{Y_{\mathrm{abd}} + \left\{\left(Y_{\mathrm{bda}} + Y_{\mathrm{beg}}\right)^{-1} + \left(D_{\mathrm{f}} + Y_{\mathrm{dab}} + Y_{\mathrm{egd}}\right)^{-1} + Y_{\mathrm{gde}}\right\}^{-1}} + \frac{1}{D_{\mathrm{c}}}\right]^{-1} + R_{\mathrm{g\_in}} \quad (2)$$

$$Z_{\mathrm{GSS}} = \left[\frac{1}{\left\{\frac{1}{Y_{\mathrm{bda}} + Y_{\mathrm{deg}} + \left\{\left(Y_{\mathrm{gde}}\right)^{-1} + \left(D_{\mathrm{f}} + Y_{\mathrm{egd}}\right)^{-1}\right\}^{-1}} + \frac{1}{Y_{\mathrm{dab}}}\right\}^{-1} + Y_{\mathrm{abd}}} + \frac{1}{D_{\mathrm{c}}}\right]^{-1} + R_{\mathrm{g\_in}} \quad (3)$$

agreement indicates that the measurements of Z_{DS}, Z_{GSO}, and Z_{GSS} can experimentally determine $R_{\mathrm{g\_in}}$.

The revised method was also applied to SCT2080KE (ROHM Company Ltd.), which is the same generation of SCT2450KE [19] and different rated drain current [20]. $R_{\mathrm{g\_in}}$ for SCT2080KE was 5.0 Ω using the revised method, smaller than the values of 6.3 Ω shown on the datasheets. E_{r} of SCT2080KE was 0.18, close to 0.20 of SCT2450KE. This shows that the revised method is applicable to other SiC MOSFETs.

VI. Conclusion

The widely utilized conventional measurement of $R_{\mathrm{g\_in}}$ does not provide a genuine $R_{\mathrm{g\_in}}$ for SiC MOSFETs because it ignores the relatively large R_{sp} in the transistors. We determined R_{sp} using the TLM method and the results were verified using the impedance characteristics of the DS and GS. This validated that $R_{\mathrm{g\_in}}$ accurately reproduces the measured switching waveforms in the DPT of the SiC MOSFET. An unsatisfactory aspect of this method is that it requires knowledge of the structure of the target device. Accordingly, to resolve this problem, we developed another measurement scheme for $R_{\mathrm{g\_in}}$ that does not require prior knowledge of device structures. $R_{\mathrm{g\_in}}$ obtained using this revised measurement scheme is very close to that of the first scheme. This facilitates the design optimization of power supplies using SiC MOSFETs.

References

[1] T. Kimoto, "Material science and device physics in SiC technology for high-voltage power devices," *Jpn. J. Appl. Phys.*, vol. 54, no. 4, Mar. 2015, Art. no. 040103, doi: 10.7567/JJAP.54.040103.

[2] J. A. Cooper, M. R. Melloch, R. Singh, A. Agarwal, and J. W. Palmour, "Status and prospects for SiC power MOSFETs," *IEEE Trans. Electron Devices*, vol. 49, no. 4, pp. 658–664, Apr. 2002, doi: 10.1109/16.992876.

[3] L. Ran, S. Gokani, J. Clare, K. J. Bradley, and C. Christopoulos, "Conducted electromagnetic emissions in induction motor drive systems. I. Time domain analysis and identification of dominant modes," *IEEE Trans. Power Electron.*, vol. 13, no. 4, pp. 757–767, Jul. 1998, doi: 10.1109/63.704152.

[4] JEDEC. *JESD24-11, Power MOSFET Equivalent Series Gate Resistance Test Method*. Accessed: May 30, 2022. [Online]. Available: https://www.jedec.org/standards-documents/docs/jesd-24-11

[5] Rohm. (May 25, 2023). *SCT2450KE*. [Online]. Available: https://fscdn.rohm.com/en/products/databook/datasheet/discrete/sic/MOSFET/sct2450ke-e.pdf

[6] Y. Mukunoki et al., "Modeling of a silicon-carbide MOSFET with focus on internal stray capacitances and inductances, and its verification," *IEEE Trans. Ind. Appl.*, vol. 54, no. 3, pp. 2588–2597, Jun. 2018, doi: 10.1109/TIA.2018.2796587.

[7] M. Shintani, Y. Nakamura, K. Oishi, M. Hiromoto, T. Hikihara, and T. Sato, "Surface-potential-based silicon carbide power MOSFET model for circuit simulation," *IEEE Trans. Power Electron.*, vol. 33, no. 12, pp. 10774–10783, Dec. 2018, doi: 10.1109/TPEL.2018.2805808.

[8] T. Yanagi and K. Nakahara, "Switching behavior method to estimate the intrinsic gate resistance of a transistor by using the gate plateau voltage," in *Proc. IEEE Energy Convers. Congr. Expo. (ECCE)*, Sep. 2019, pp. 1998–2000, doi: 10.1109/ECCE.2019.8913057.

[9] K. Han and B. J. Baliga, "Comprehensive physics of third quadrant characteristics for accumulation- and inversion-channel 1.2-kV 4H-SiC MOSFETs," *IEEE Trans. Electron Devices*, vol. 66, no. 9, pp. 3916–3921, Sep. 2019, doi: 10.1109/TED.2019.2929733.

[10] T. Tominaga et al., "Body potential control via p-type contact resistance and its influence on switching characteristics of 4H-SiC MOSFETs," *IEEE Trans. Electron Devices*, vol. 69, no. 1, pp. 285–290, Jan. 2022, doi: 10.1109/TED.2021.3130863.

[11] B. J. Baliga, *Fundamentals of Power Semiconductor Devices*. New York, NY, USA: Springer, 2008, pp. 82–83.

[12] D. K. Schroder, *Semiconductor Material and Device Characterization*. Hoboken, NJ, USA: Wiley, 2006, pp. 138–149.

[13] *SentaurusTM Device User Guide: Version P-2019.03*, Synopsys, Inc., Mountain View, CA, USA, 2019.

[14] M. Kocher, M. Rommel, P. P. Michałowski, and T. Erlbacher, "Mechanisms of ohmic contact formation of Ti/Al-based metal stacks on p-doped 4H-SiC," *Materials*, vol. 15, no. 1, p. 50, Dec. 2021, doi: 10.3390/ma15010050.

[15] S. Ogawa, T. Tanaka, Y. Nakamura, and K. Nakahara, "Anisotropic temperature distribution causing an incremental trend in the saturated drain-current of SiC MOSFET," in *Proc. Extended Abstr. Int. Conf. Solid State Devices Mater.*, Sep. 2020, pp. 233–234, doi: 10.7567/SSDM.2020.D-6-02.

[16] J. Wang and B. W. Williams, "A simulation study of high voltage 4H-SiC IGBTs," *Semicond. Sci. Technol.*, vol. 13, no. 7, pp. 806–815, Jul. 1998, doi: 10.1088/0268-1242/13/7/026.

[17] Y. Nakamura, N. Kuroda, T. Yanagi, H. Sakairi, and K. Nakahara, "High-voltage and high-current I_{d}–V_{ds} measurement method for power transistors improved by reducing self-heating," *IEEE Electron Device Lett.*, vol. 41, no. 4, pp. 581–584, Apr. 2020, doi: 10.1109/LED.2020.2974492.

[18] H. Sakairi, T. Yanagi, H. Otake, N. Kuroda, and H. Tanigawa, "Measurement methodology for accurate modeling of SiC MOSFET switching behavior over wide voltage and current ranges," *IEEE Trans. Power Electron.*, vol. 33, no. 9, pp. 7314–7325, Sep. 2018, doi: 10.1109/TPEL.2017.2764632.

[19] Rohm. (May 25, 2023). *Trench-Structure SiC-MOSFETs and Actual Products*. [Online]. Available: https://techweb.rohm.com/product/power-device/sic/sic-basic/6574/

[20] Rohm. (May 25, 2023). *SCT2080KE*. [Online]. Available: https://fscdn.rohm.com/en/products/databook/datasheet/discrete/sic/mosfet/sct2080ke-e.pdf